

PAPER • OPEN ACCESS

## Magnetic array-templated method for fabrication of polymer nanoporous films

To cite this article: Jarryd Keng Gene Ng *et al* 2020 *Nano Express* 1 010044

View the [article online](#) for updates and enhancements.



## PAPER

## Magnetic array-templated method for fabrication of polymer nanoporous films

## OPEN ACCESS

RECEIVED  
5 February 2020REVISED  
27 April 2020ACCEPTED FOR PUBLICATION  
27 May 2020PUBLISHED  
9 June 2020

Original content from this work may be used under the terms of the [Creative Commons Attribution 4.0 licence](#).

Any further distribution of this work must maintain attribution to the author(s) and the title of the work, journal citation and DOI.

Jarryd Keng Gene Ng<sup>1,2</sup>, Sergey I Rybchenko<sup>1</sup> and Sergei Lukaschuk<sup>1</sup><sup>1</sup> Department of Engineering, University of Hull, Hull, HU6 7TY, United Kingdom<sup>2</sup> Presently with Agilent Technologies, Bayan Lepas Free Industrial Zone, 11900, Penang, MalaysiaE-mail: [s.i.rybchenko@hull.ac.uk](mailto:s.i.rybchenko@hull.ac.uk)**Keywords:** colloidal particles, directed self-assembly, nano-patterning, nanopores, polymer membranes, ionic conductivity**Abstract**

This paper describes the development of a novel method of producing nanoporous polymeric membranes in a cost-effective and reproducible manner. The novelty of the technique hinges on the exploitation of a new type of sacrificial material & structures - self-assembled arrays of magnetic nanoparticles. The arrays are obtained through application of an external magnetic field to a thin layer of colloidal solution of superparamagnetic nanoparticles in a polymerizable monomer; this is followed by photopolymerisation. The resulting columnar structures form the pore templates which when selectively etched away leave an array of nanopores spanning across the polymeric film. The morphological characterisation of the nanopores by scanning electron microscopy and ionic conductivity revealed a very unusual sponge-like pore morphology. The applications which would benefit from the specific pore morphology and arrayed manufacturing are discussed.

**1. Introduction**

Nanoporous materials have been shown to have applications in a number of multidisciplinary fields [1–9]. Nanopores with a size ranging from 1 nm to 100 nm have been widely used in recent years as highly sensitive sensors that can detect various molecules, biospecies and nanoparticles in aqueous solution. Highly selective membranes, selective adsorbents, electrodes for fuel cells, and various sensors are among the most popular applications for nanoporous polymers in particular [2, 4]. One large area is biochemical and biomedical applications. Here the low cost and ease of synthesis of polymers is combined with their biodegradability and biocompatibility, which are key characteristics for cell and tissue engineering. The popular applications include biofiltration, immunoisolation, and drug delivery [3]. Nanoporous polymeric materials have also received much attention as materials of choice in smart applications [8], in particular as sensors for environmental control and monitoring [9] as well as in controlled release systems [7]. Contemporary fabrication of nanostructured polymers is often based on photolithography, nanoimprint pattern-transfer, block copolymer self-assembly, track etching, and solvent-based formation [4–6]. Development of bottom-up approaches involving the self-assembly of molecular and colloidal building blocks, or phase-separation is probably the most promising way to produce novel nanoporous membranes and coatings at lower cost and higher throughput than top-down strategies. In particular, fabrication of polymer nano- and microstructures by making use of colloidal self-assembled templates has shown a large progress in developing a variety of flat 2D-like structures [5, 6].

This work is a continuation in development of bottom-up techniques, where we studied the new version of nanopore templating based on self-assembly of magnetic nanoparticles into truly 3D structures. Our approach could be seen as a variation of the preparation method based on selective removal of a sacrificial template material from an insoluble matrix. The sacrificial material in our case is the assembly of parallel arrays composed of magnetite nanoparticles. The arrays are created via the nanoparticles self-assembly process under application of an external magnetic field, which is well-known from the studies of ferrofluid emulsions [10–16]. Normally these emulsions are water based, but it has been shown that nanoparticles can be dispersed in other liquids including polymerizable monomers such as 1,6-hexanediol diacrylate (HDDA) or styrene [11, 12]; this allows

solidifying of the liquid layer with the arrays assembly embedded into it. The idea behind this study is that selective etching of the embedded arrays will produce a polymeric film with an assembly of aligned hollow channels, i.e. a porous membrane. It has already been shown in [17], that the embedded arrays make good electrical contact with the confining plates allowing for array conductivity to be evaluated. This suggests an existence of a good mechanical contact between the array tip and the plate, which means that etching off the array via pore opening at the contact point is possible.

Magnetite nanoparticles used in our work and in the past publications are superparamagnetic at room temperature, which allows them to be dispersed to form colloids. But under application of an external magnetic field, the net magnetic moment is stabilised at each nanoparticle, causing interaction between them. This dipolar interaction results in chaining of the nanoparticles in the field direction. In turn, the magnetostatic interaction between the chains drives aggregation of them into thicker columnar arrays. If the original colloidal solution was confined into a thin layer, a regular 2D distribution of parallel columnar arrays spanning across the entire layer thickness is obtained [10–16].

One of the first theoretical models established a scaling relationship between the inter-array separation ( $\lambda$ ) and layer thickness (array length) ( $L$ ) as  $\lambda \propto L^{1/3}$  from basic energy balance analysis [16]. Subsequently, this scaling relationship was generally confirmed in a number of experimental studies and theoretical models [10–15], although there was no agreement on the value of power-law exponent ( $\alpha$ ). The predicted  $\alpha = 0.33$  was found [10] to be a reasonable approximation for thin films ( $L \ll 100 \mu$ ), while for the thicker films ( $L > 100 \mu$ )  $\alpha \approx 0.5$  [9] or even  $\alpha \approx 1$  [15] were obtained. These studies also confirmed that  $\lambda$  is not sensitive to the nanoparticles volume fraction ( $\phi$ ). At larger  $\phi$ , the columnar arrays tend to grow thicker instead of increasing in numbers. In particular, in one of the most detailed experimental studies Liu and co-workers [10], have established that  $\lambda$  was fixed between 6 and 8  $\mu$  for  $\phi$  varied in 0.03–0.3 range for  $L = 100 \mu$ . They have also shown for  $L < 100 \mu$  and  $\phi = 0.04$  the scaling relationship is:

$$\lambda = 1.33L^{0.37} \quad (1)$$

Importantly for our study, these findings allow predicting the pores (arrays) volume fraction and density.

## 2. Materials and methods

### 2.1. Materials

Ferric chloride hexahydrate ( $\text{FeCl}_3 \cdot 6\text{H}_2\text{O}$ , 97%), ferrous chloride tetrahydrate ( $\text{FeCl}_2 \cdot 4\text{H}_2\text{O}$ ), isopropyl alcohol (99.5%), and ammonium hydroxide ( $\text{NH}_4\text{OH}$ , 33 wt.%) were purchased from Fisher Scientific, UK. Oleic acid (99%), photo-polymerizable organic oil (1,6-hexanediol diacrylate (HDDA),  $\geq 95\%$ ) and the UV sensitizer Darocur-1173 (97%) were procured from Sigma-Aldrich, UK. For all solutions and rinsing a Milli-Q water ( $18.2 \text{ M}\Omega \text{ cm}^{-1}$ ) has been used.

### 2.2. Methods

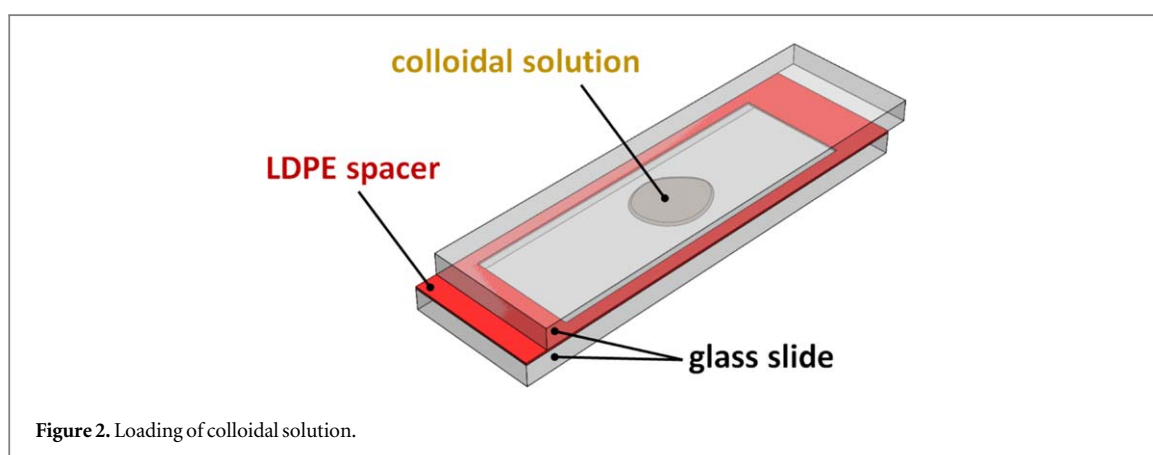
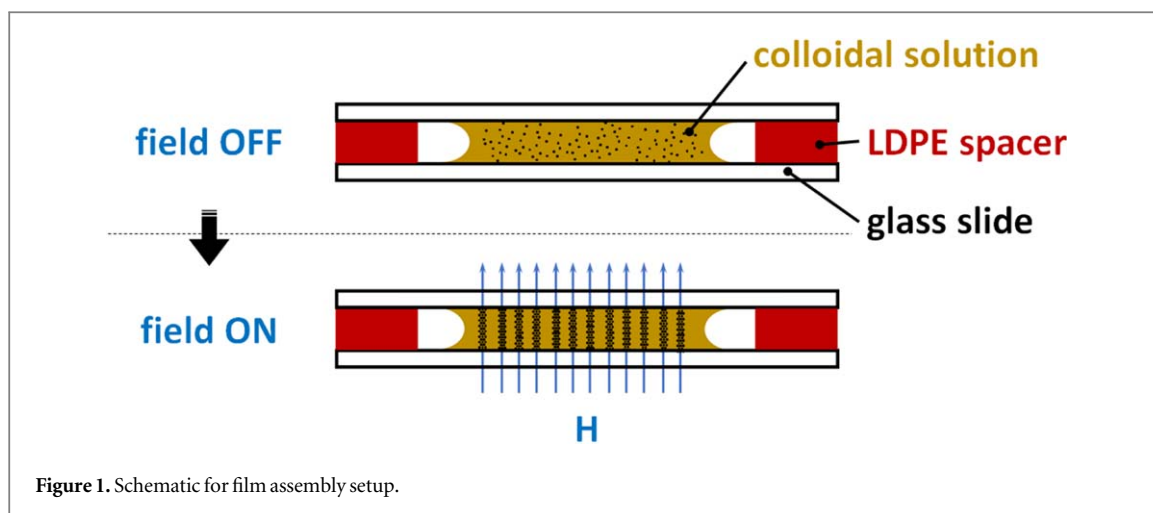
$\text{Fe}_3\text{O}_4$  nanoparticles were synthesised using established method [18] also used in [17]. This encompassed the co-precipitation from aqueous solution of ferric and ferrous salts by addition of a base. The ferric chloride hexahydrate and ferrous chloride tetrahydrate were dissolved in de-oxygenated Milli-Q water to obtain  $\text{Fe}^{3+}$  and  $\text{Fe}^{2+}$  molar ratio of 1.75:1. The solution was heated for 1 h in a nitrogen atmosphere at 80 °C while being stirred. Then ammonia solution was added in excess along with oleic acid to induce the precipitation. The resulting suspension was vigorously stirred for another hour at the same temperature and then cooled to room temperature under protective atmosphere. The precipitated particles were rinsed five times with Milli-Q water till neutral pH was achieved, separated via magnetic decantation and subsequently rinsed with isopropyl alcohol. The nanoparticles in this state were then dispersed in HDDA sensitised with Darocur at 0.5 wt%. The resultant solution was ultrasonically agitated at 20 kHz for 30 min to form the final colloidal solution. The volume fraction of the nanoparticles was fixed at 5%.

Radiation ( $\sim 1 \text{ mW cm}^{-2}$ ) from a 100-W high-pressure mercury lamp was used as the UV source for the photo-polymerization, which was conducted in a dry nitrogen gas atmosphere.

Ion milling procedure was conducted using the precision ion polishing system from Gatan Precision Ion Polishing System (PIPS™). The milling procedure was carried out in pulsed mode at 2 keV and 25  $\mu\text{A}$ , using a rotational speed of 6 rpm at a milling angle of 10°.

### 2.3. Characterisation

The nanoparticles were characterised by transmission electron microscopy (TEM) analysis confirming their average size to be  $\sim 10 \text{ nm}$ . For that, a drop of nanoparticles solution in methanol was casted on carbon-coated TEM grid. After complete evaporation of methanol, the grid with deposited nanoparticles was viewed on JEOL



2010 TEM. Zeiss EVO60 and Cambridge S360 Scanning Electron Microscopes (SEM) equipped with INCA Energy Dispersive Spectroscopy (EDS) feature were used for morphological studies. For SEM observations, a gold coating of 10–15 nm was deposited on all HDDA samples by using a vacuum evaporator. Optical images were obtained with Leica DM4000 microscope equipped with digital camera.

### 3. Results and discussion

#### 3.1. Template production and characterisation

As a first step, the superparamagnetic nanoparticles covered with oleic acid are synthesised and dispersed (at 5 vol.%) in photo-polymerizable organic oil (HDDA). Next, a system of parallel arrays is assembled from these nanoparticles. The assembling setup (shown in figure 1) was an adaptation of that described in [17]. A small volume of the colloidal solution was deposited onto a borosilicate glass slide which was confined by another slide of similar dimensions to shape the volume into a circular puddle (see figure 2). These slides were kept separated via spacers made of low-density polyethylene (LDPE) which fixes a distance between them. The slide assembly was placed in an air-tight enclosure and purged with nitrogen gas.

The self-assembly is initiated by gradual application of an external magnetic field to the confined solution (see figure 1). The field was raised at a rate of  $2 \text{ mT s}^{-1}$  up to 5 mT and kept at this value for 5 min. Columnar arrays of nanoparticles parallel to the field direction were created as a result, which was confirmed *in situ* by optical microscopy. Once the array assembly was completed, *in situ* UV photo-polymerisation of the HDDA matrix was performed while the magnetic field was still on. This ensures immobilisation of the arrays in the polymer matrix. A typical sample has a film of  $\sim 3 \text{ mm}$  in diameter and thickness was fixed at  $\sim 10 \mu\text{m}$  for the majority of the samples used for this study.

The in-plane distribution of the nanoparticle arrays is illustrated by the optical microscopy images in figure 3 (top glass slide removed). On this bright-field image, the arrays appear as dark spots. Although some clustering of arrays is present, all arrays are well separated as expected from the repelling dipolar interaction governing the self-assembly process. From statistical analysis of the optical images, the inter-array spacing was evaluated, using

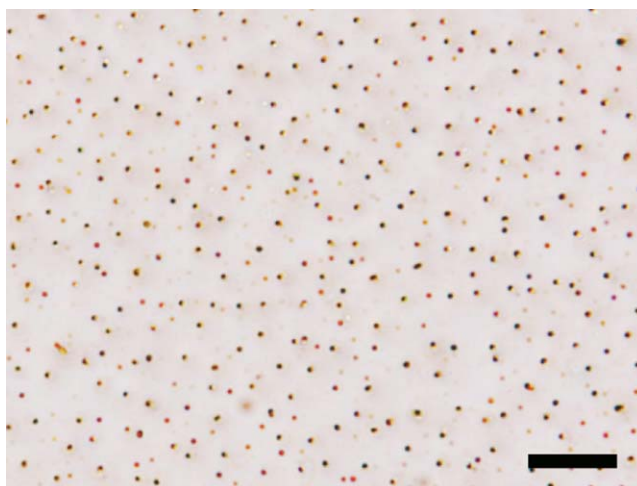


**Figure 3.** Top-view optical microscopy image of the in-plane distribution of the nanoparticles arrays in polymerised film. Top glass slide removed. Scale bar is 20  $\mu\text{m}$ .

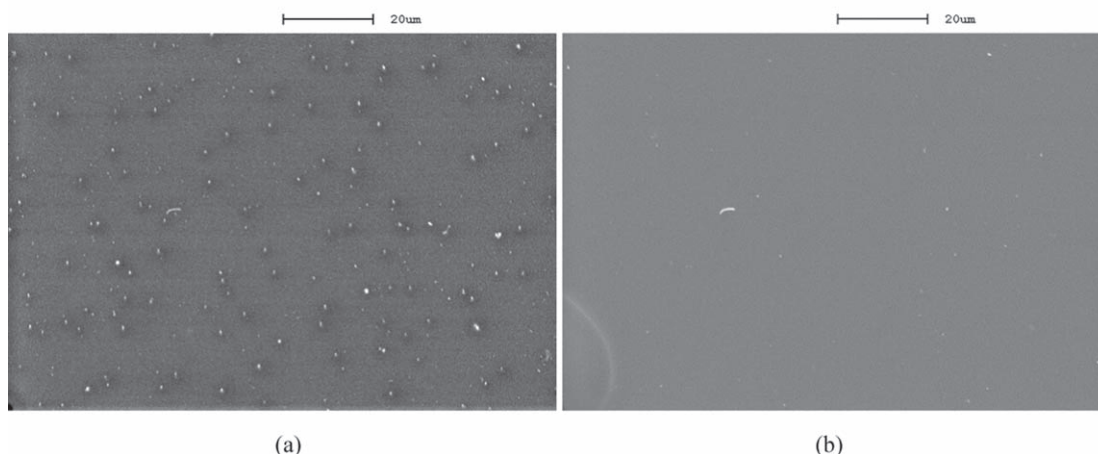
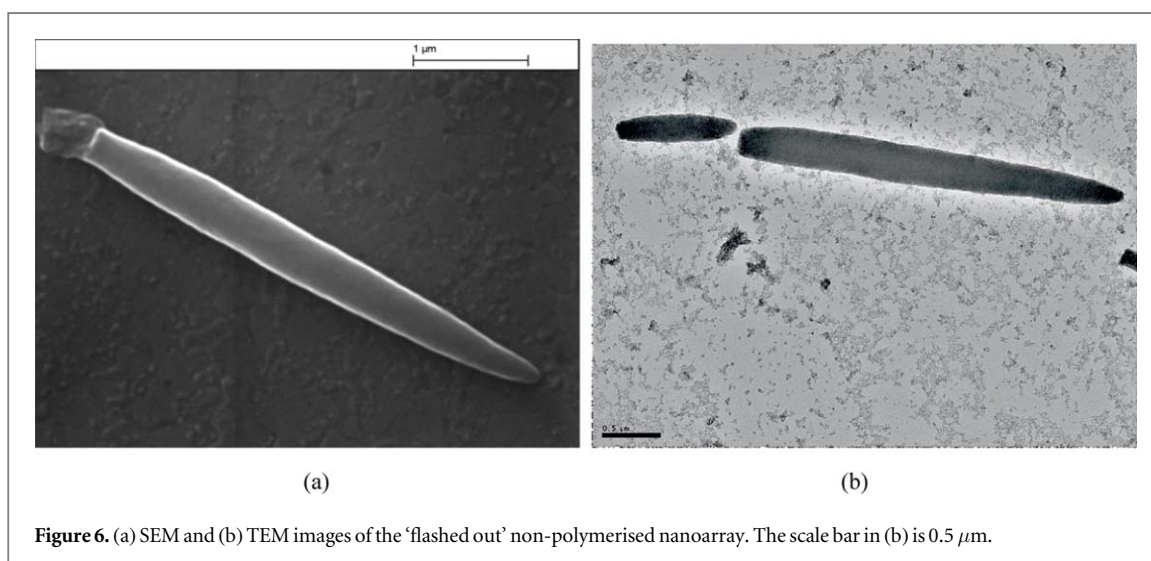
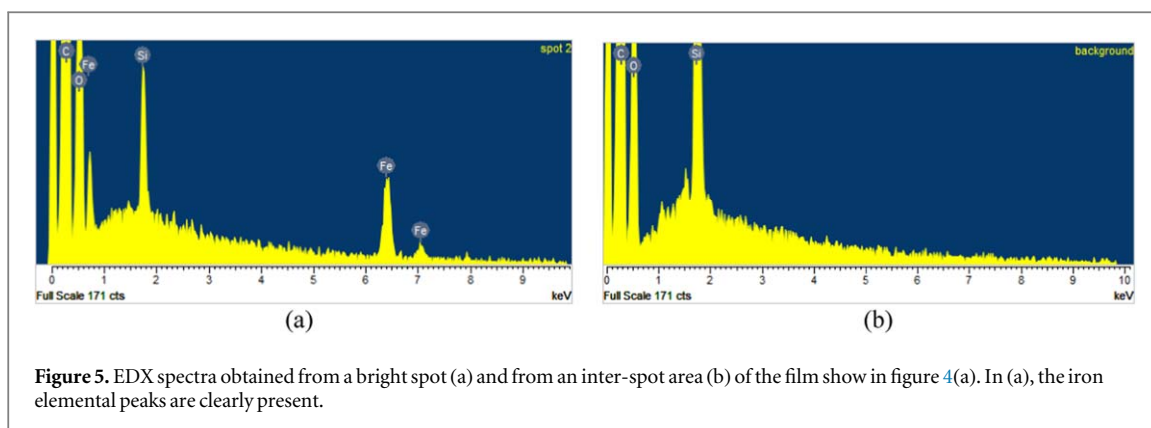


**Figure 4.** Top-view SEM images of the same part of polymerised film obtained in secondary electron (a) and back-scattered electron (b) imaging modes.

the radial average autocorrelation function provided by ImageJ software. The value of  $3.2 \pm 0.7 \mu$  was obtained for the first correlation maximum, which is in good agreement with  $3.1 \mu$  inter-array separation value predicted from equation (1) for a film (layer) thickness of  $10 \mu$ . The agreement indicates that equation (1) satisfactorily describes the array parameters in our case. On the other hand, the statistical analysis also involved the weaker contrast dots, associated with shorter arrays attached to one surface of the film. These arrays are apparently contributing to the dipolar interactions stabilising the entire array assembly, but they are not spanning across the whole film thickness and hence do not contribute to the pore production. Thus, to obtain a realistic density of the arrays (pores) propagating through the film we have discarded short arrays via intensity threshold discrimination in image analysis. The array density obtained in this way was found to be  $1 \pm 0.5 \times 10^6 \text{ per cm}^2$ , averaged over 60 images across 5 samples.

Figure 4 shows SEM images of the polymerised film obtained in secondary electron and back-scattered electron imaging modes. The image obtained in back-scattered electrons (figure 4(b)) shows largely featureless film surface (except dust). But secondary electron image (figure 4(a)) allows revealing the subsurface features of the film due to element-sensitive contrast. In these images, the arrays appeared as bright spots. The EDX spectra obtained from such bright spots and the inter-spot area are shown in figure 5. The appearance of iron element peaks in the spectrum (figure 5(a)) confirms the iron oxide-enriched composition of the bright spots.



### 3.2. Individual array morphology

Pore morphology is expected to be defined by the nanoarray template. The geometry of the nanoarrays embedded in the polymer is difficult to access with either optical microscopy (not enough resolution) or electron microscopy (films are not transparent to electrons). Hence the expected nanopore geometry was judged from the images of the ‘flushed out’ non-polymerised nanoarrays shown in figure 6. To produce this kind of sample, we used the fact that arrays can be self-assembled in a free layer of the colloidal solution, not covered by the top glass slide. The arrays were assembled in such a layer under magnetic field applied in the usual way. After assembly, the magnetic field was switched off and the non-polymerised solution was quickly washed off with acetone. The slide (or carbon-coated TEM grid) with whatever deposited arrays remained was immediately placed in dynamic vacuum for 3 h and subsequently transferred to the SEM (TEM) chamber for analysis. The arrays were not polymerised and hence could be deformed during the preparation, i.e. flattened. They also come in a range of sizes reflecting the gradient of the solution layer thickness, but they still provide a good estimate of the shape and size of the original arrays. The arrays shown in figure 6(a) has tapered ends and the mid-length thickness (diameter) of  $\sim 400$  nm at a length of  $4.5 \mu$ . Similar array in TEM image (figure 6(b)) displays homogeneous distribution of the nanoparticles inside it. These morphological features are in agreement with a scaled down version of the microarrays of magnetic nanoparticles normally obtained in ferrofluids [10–15].

### 3.3. Nanopores membranes production and characterisation

The self-assembled arrays described above were intended to serve as templates for nanopore production. The nanopores were obtained by etching the nanoparticles out of the nanoarrays. This was achieved by removing the confining glass plate(s) and soaking the polymer film in the 2M HCl solution for 24 h at room temperature. To remove the polymerised film from the glass slides, a few droplets of isopropanol were deposited onto the film area and left to soak for 30 min in order to dislodge the film from the substrate. In some cases, soaking for a short time ( $\sim 3$  min) in boiling Milli-Q water was used to encourage film separation from the glass slides. The etched films were rinsed in deionised water and dried with a nitrogen gas stream. Comparative analysis of the optical images of the films before and after etching shows (figure 7) that the majority of the black spots have

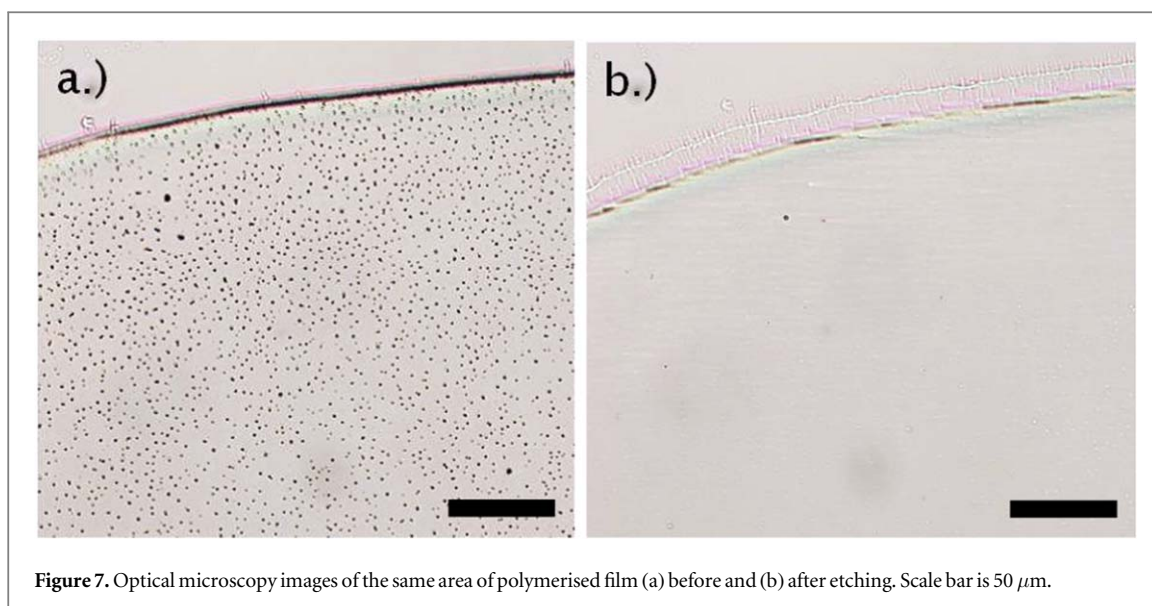


**Figure 7.** Optical microscopy images of the same area of polymerised film (a) before and (b) after etching. Scale bar is 50  $\mu\text{m}$ .

disappeared. The successful etching of the nanoarrays indicates that they have an opening to the film surface. Exposing only one side of the polymer film to the etching solution confirms that about 20% of the pores starting at one surface of the film do not extend through to the opposite surface. The latter finding correlated with the outcome of the statistical analysis of optical images of unetched arrays.

SEM surface imaging was conducted to estimate the size of the nanopore opening to the film surface. As the HDDA film is a dielectric, the 10–15 nm gold coating has to be applied to the film before the SEM analysis. Typical SEM images are presented in figure 8. Depressions are shown at the expected pore opening spot, reflecting the compressive strain relaxation after removal of the arrays. However, on their bottom, the depressions do not exhibit any pore opening, contrary to initial expectations. A detailed survey of several batches of samples was conducted but no evidence for a pore opening was obtained. The surface morphology was found to be essentially featureless down to the level of the gold coating inhomogeneity, as shown in figure 8(c). This result indicates that the pore opening size must be smaller than the gold coating thickness (10–15 nm) and the coating is masking the openings.

We have used ion-beam milling to prepare the nanopore transverse cross sections. Ar-ion beams are known to be destructive for polymer samples, causing severe heating and even melting [19]. In order to eliminate these issues, we tuned the ion gun on the PIPS machine down to the lowest acceleration voltage and current available and enabled the pulsed mode. The milling geometry is illustrated in figure 9. The SEM images in figure 10(a) show the top surface of the film after in-plane thinning of the sample to approximately half of original thickness. On this image, the dark spots (0.3–0.5  $\mu\text{m}$  in diameter) are presumably representing the nanopore cross section. But the density of these spots is much less than the typical nanopore density. This discrepancy is likely to be a result of the sample overheating and local melting during the milling, which sealed the majority of the pores. At the perpendicular walls of cracks and cuts in the sample, however, the milling conditions appear to be much milder. Here we have found the nanopores axial cross sections as shown in figures 10(b)–(d). The internal morphology of the nanopore appears as a porous structure composed of the 20–50-nm diameter cavities interconnected into some sort of labyrinth. A reconstructed internal morphology of the nanopores is sketched in figure 11. Since this morphology of the nanopore differs significantly from that of the unpolymerized array (see figure 6), we prepared a micropore sample to check the pore morphology in details.

### 3.4. Micropore samples

Important information regarding the general trends in internal morphology of the nanopores can be gathered from studies of upscaled membranes obtained by the same technology. Membranes with the film thickness  $L$  of hundreds of microns were successfully fabricated using the same volume fraction of the nanoparticles ( $\phi = 0.04$ ). For this thickness, the film is self-supporting and hence a clear parallel cross section can be easily obtained by cryo-cracking. The representative images of the micropores in the 150  $\mu\text{m}$  film is presented in figure 12. The pores reach  $\sim 10 \mu\text{m}$  in the middle cross-section. The internal morphology of the pore has a foam-like cellular structure composed of interconnected voids of different sizes. The larger cavities appear in the core part of the pore and the smallest cavities are decorating the interface between the pore and the bulk of the film. The pore opening to the surface is also composed of smaller cavities. It is interesting that the size of the smallest cavities is similar to the size of the cavities shown for the nanopore cross section in figure 10(d). The pronounced

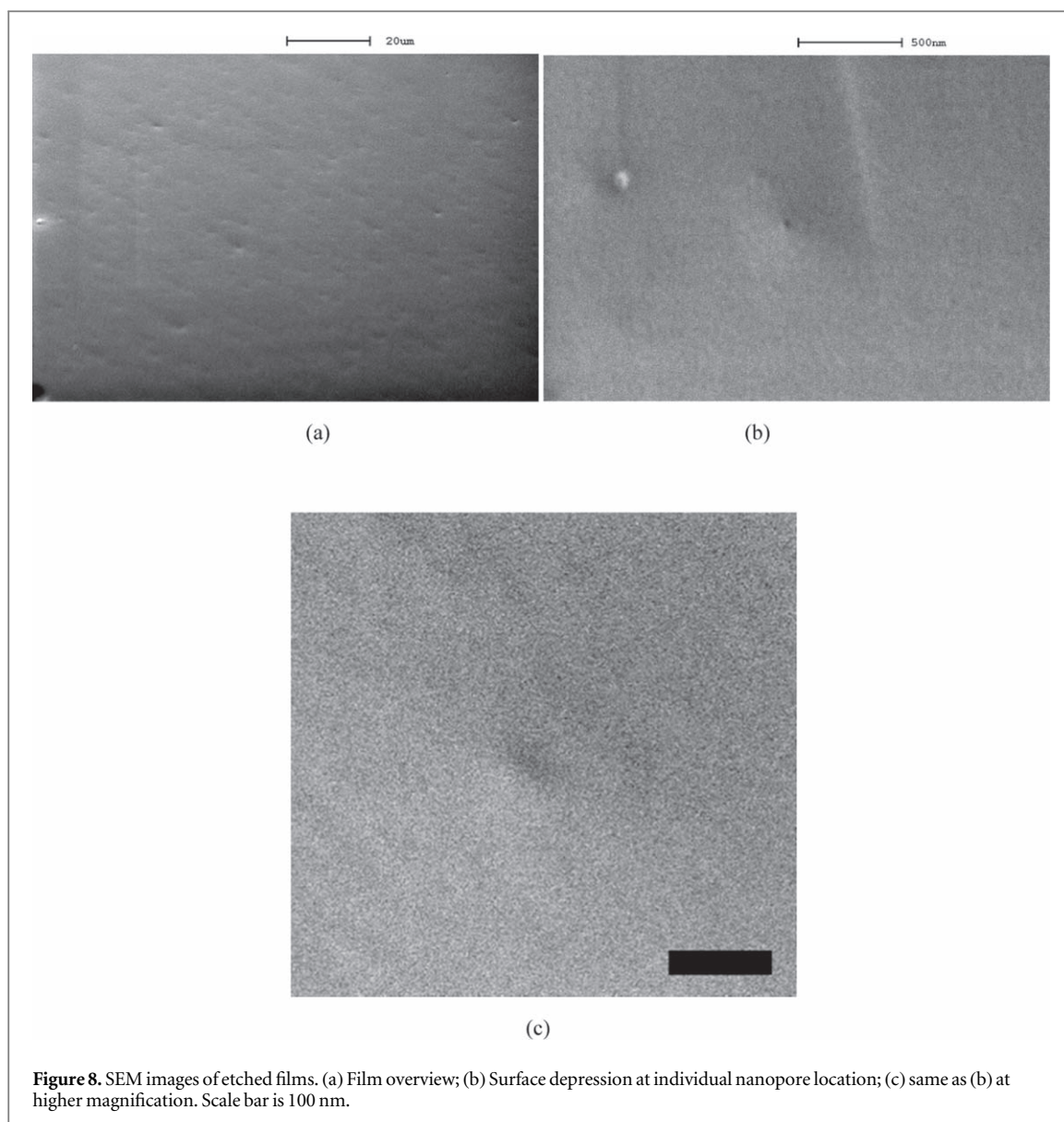


**Figure 8.** SEM images of etched films. (a) Film overview; (b) Surface depression at individual nanopore location; (c) same as (b) at higher magnification. Scale bar is 100 nm.

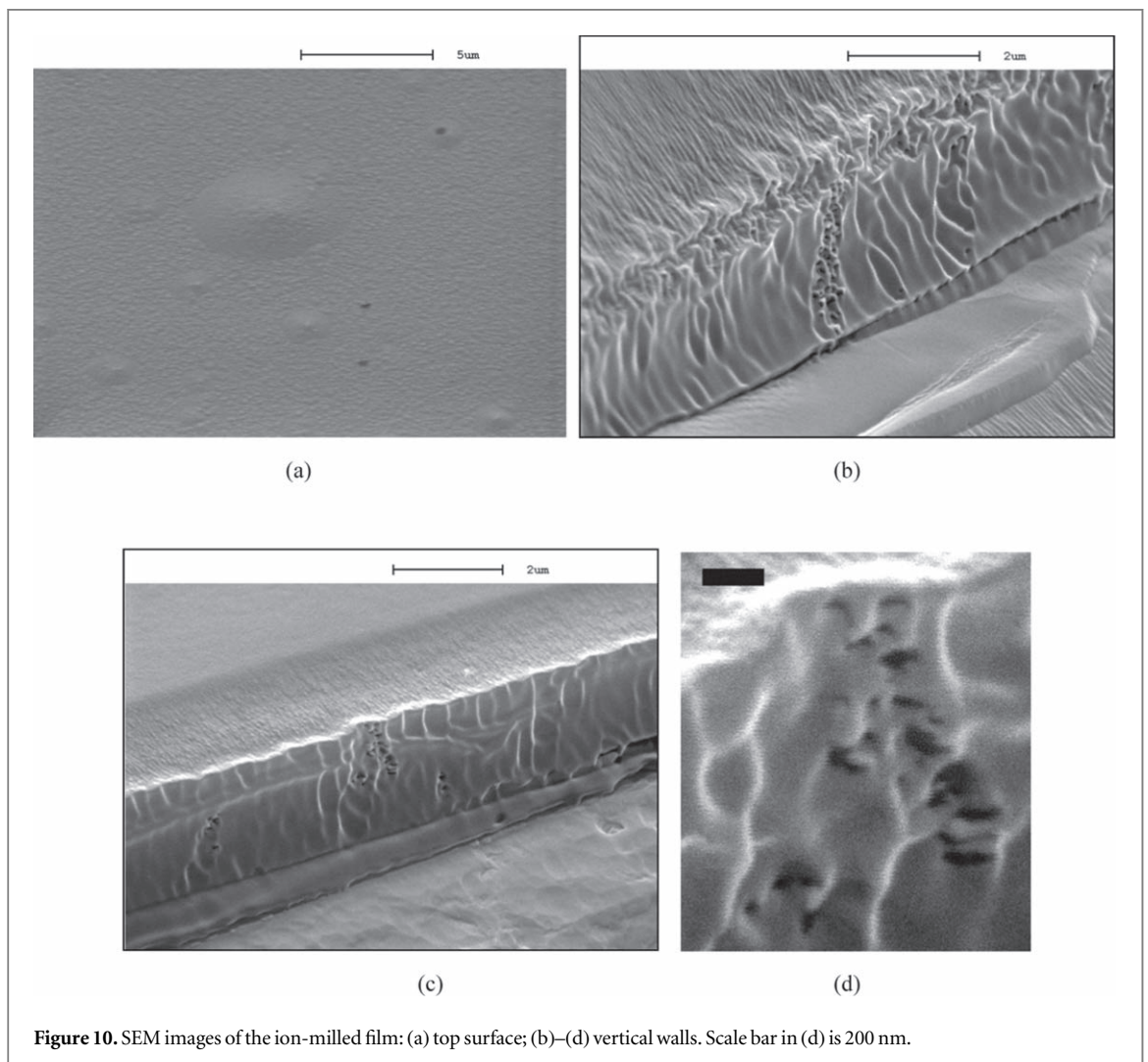
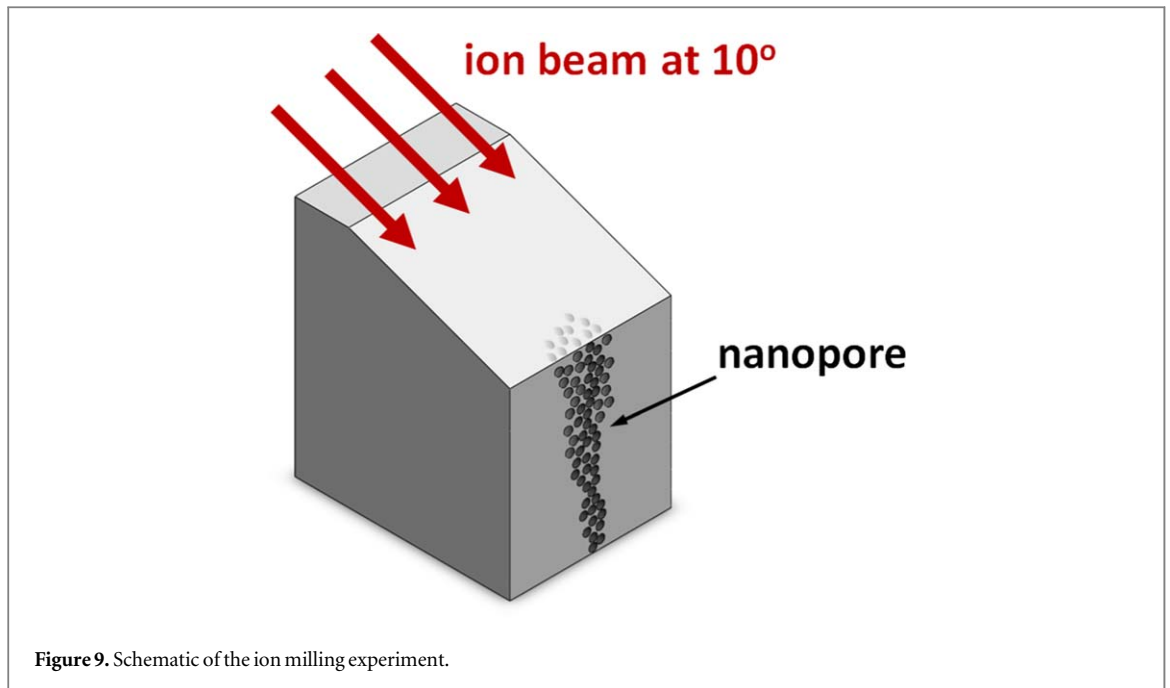
dip at the pore opening is also observed (see figure 12(c)). In general, ignoring the voids size hierarchy, the micropores have a cellular type of inner structure, which resembles the nanopore inner morphology exposed in figures 10(b)–(d). This strengthens the conclusion that figure 11 gives a good approximation to the true nanopore structure.

The mechanism by which the cellular structure appears is not clear. Since the local photo-polymerisation rate is proportional to the local intensity of the UV light, some sort of continuous gradient polymerisation front moving inside the array can be expected, reflecting the decay of the UV light intensity inside the array. The observed foam-like cellular morphology could be seen as a result of instability of the polymerisation front induced by compressive mechanical stress accompanying polymerisation. The largest clusters observed in the core of the micropore could also be the result of under-polymerisation due to insufficient UV exposure, or alternatively they could be a result of squeezing any excess oleic acid into the middle part of the array as the polymerisation proceeds. More research is required to establish a mechanism of the cellular structure formation.

### 3.5. Ionic conductivity measurements

Ionic conductivity is a direct method of assessing the transport properties of nanopores [20], which is a core to many applications. It is also used for independent evaluation of the nanopore dimensional parameters, complementing the electron microscopy characterisation.

A schematic illustration of the setup for the ionic conductivity experiments is presented in figure 13. The nanopore membrane was glued onto the acetate diaphragm using LOCTITE 0151 Hysol<sup>®</sup> epoxy adhesive. The diaphragm has an opening of 1 mm diameter, which defines the area of the membrane exposed to solution.



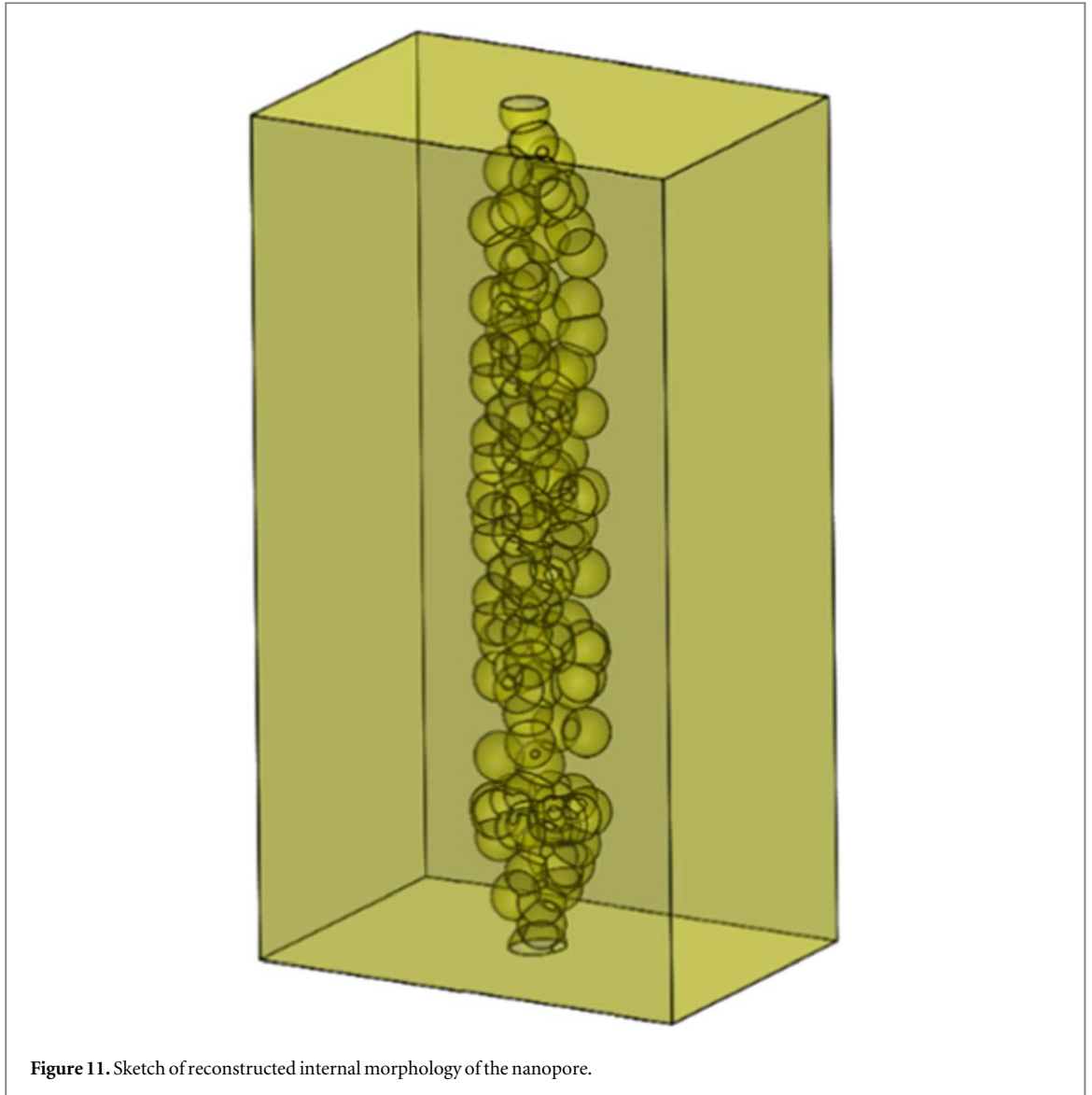


**Figure 11.** Sketch of reconstructed internal morphology of the nanopore.

Figure 14(a) displays typical  $I$ - $V$  characteristics for the nanopore membrane in 1-M KCl solution. The characteristic of a commercial Nuclepore membrane is also shown in the same graph, as a benchmark measurement. All  $I$ - $V$  data in figure 14 are recalculated per single nanopore. Test measurements with unetched membrane and with different KCl concentrations were also performed to ensure data consistency. These tests have confirmed a proportional scaling of the membrane conductivity with KCl concentration and a negligible effect of leakage current.

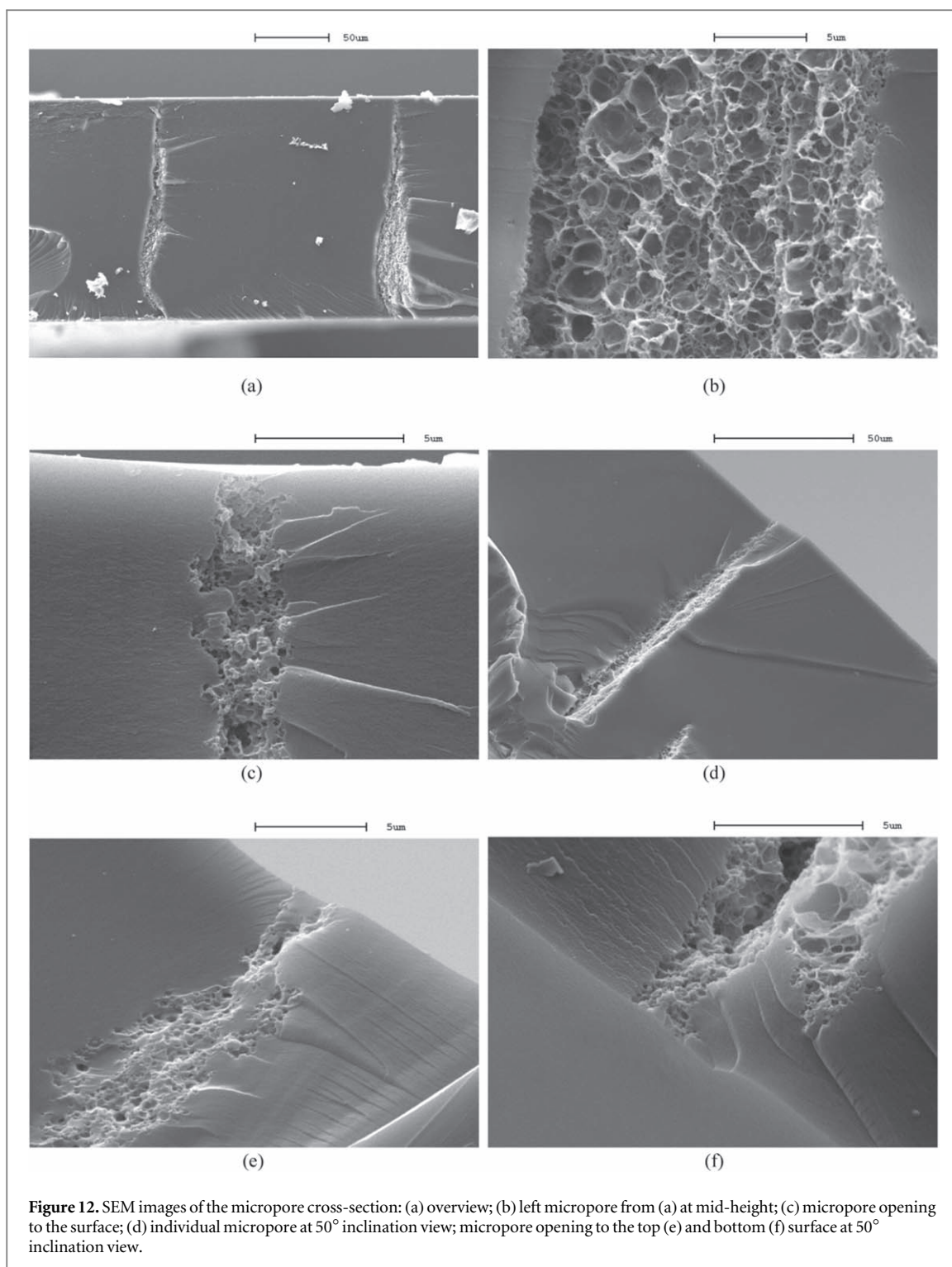
In analysis of the conductivity data, two models were employed. In the first model, the nanopore was approximated by a straight cylindrical channel of length  $L$  and diameter  $D$ . The conductivity of this nanopore is described by the following formula:

$$G_{total} = \sigma \left[ \frac{4L}{\pi D^2} + \frac{1}{D} \right]^{-1}, \quad (2)$$

where  $\sigma$  is the electrolyte conductivity. The first term in brackets reflects the resistance of the cylindrical channel and the second term is responsible for the access (spreading) resistance. Calculation results using equation (2) are shown in figure 14(b) for a range of nanopore diameters,  $D$ .

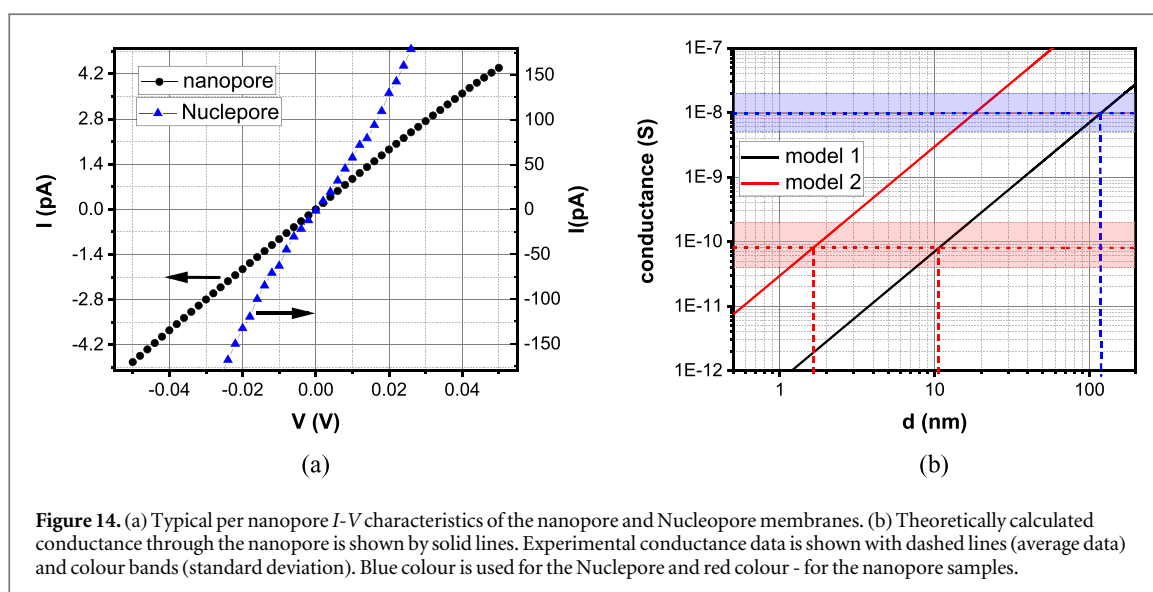
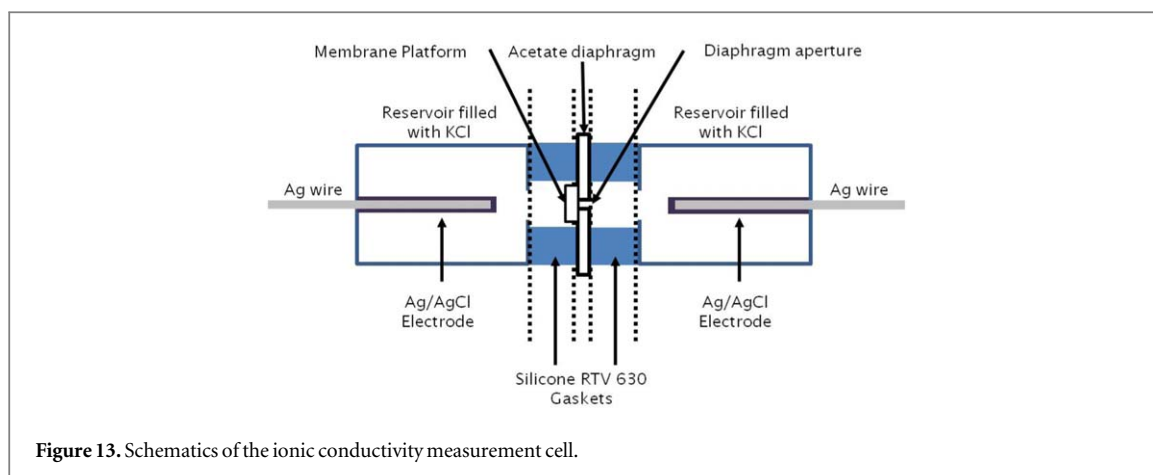
In the case of the Nuclepore membrane, the nanopore is known [21] to be a cylindrical channel of diameter 0.1  $\mu\text{m}$ , at a pore density of  $4 \times 10^8 \text{ cm}^{-2}$ . Hence the model should be well suited to that sample. Indeed, with our measurements it gives an average diameter of 116 nm and spans the range of 85–170 nm, which is in a good agreement with the membrane specification.

For the nanopore membrane, the model effectively sets the upper limit for the possible opening diameter  $D$ . Taking the nanopore density  $1 \pm 0.5 \times 10^{10} \text{ m}^{-2}$  and  $\sigma = 9.1 \text{ S m}^{-1}$  [22], the average nanopore diameter  $D = 10.5 \text{ nm}$  and span range from 7.5 to 17 nm were obtained (see figure 14(b)). The channel resistance governs



the total conductance over the whole range of  $D$  covered in figure 14(b) (as indicated by the model line slope), with access resistance being negligible. The range of 7.5–17 nm agrees with our conclusions from SEM observations, which implied that the nanopore opening is less than 10–15 nm.

The second model was set to mimic the nanopore morphology shown in figure 11. Specifically, the resistance was represented as that of series combination of several short cylindrical cavities separated by very narrow constrictions. Each constriction of diameter  $D$  contributes one access resistance. To ensure the applicability of the access resistance approximation, the diameter of each cylindrical channel was fixed at a value of  $5D$ , while the channel length was fixed at  $10D$ . The number of constricted openings is defined by the membrane thickness  $L$  ( $10 \mu$ ) and given as  $\frac{L}{10D}$ . The overall conductance is described by the following formula:



$$\begin{aligned}
 G_{total} &= \sigma \left[ \left( \frac{4 \times 10D}{\pi(5D)^2} + \frac{1}{D} \right) \times \frac{L}{10D} \right]^{-1} \\
 &= \sigma \left[ \left( \frac{1.6}{\pi D} + \frac{1}{D} \right) \times \frac{L}{10D} \right]^{-1} \\
 &= \sigma \left[ \frac{(1.6 + \pi)L}{10\pi D^2} \right]^{-1}, \tag{3}
 \end{aligned}$$

The graph of this function is shown in figure 14(b). In this model, the access resistance and cylinder resistance terms each cause a comparable effect on the total conductance. As follows from figure 14(b), this model produces  $D$  in the range of 1.2–2.6 nm, which corresponds to approximately 500 cylindrical cavities of 6–13 nm diameter. Adding extra parallel strings of cavities would lead to further reduction of  $D$  beyond 1 nm, which appears unrealistic in view of the relatively fast etching process and the soft nature of a polymer.

To conclude, the ionic conductivity analysis suggests that the nanopore can be seen as a conglomerate of interconnected cavities of 10–20 nm diameter connected by narrow openings of 1–2 nm diameter. The interconnected cavities are likely to produce just one percolating pass per nanopore on average. These conclusions agree with the morphology model developed from the microscopy studies.

### 3.6. Potential applications

The obtained nanopore density of  $10^6$  per  $\text{cm}^2$  is relatively low, which limits the films applications in high throughput filtering. Instead some other applications become possible due to the specific morphology of the nanopores. Indeed, the pore represents a network of cavities interconnected via narrow openings. The size of the cavities can be adjusted via film thickness and nanoparticle loading. The cavities can be seen as a container, offering applications in areas where the storage or processing chambers are required. One example is slow

release applications [7], where the release of the container content can also be made responsive to mechanical pressure due to the film flexibility. Delay lines in molecular sequencing and ion-exchange channels are examples from other areas [1]. Transparent nature of the films offers their application in optical detectors utilising fluorescent marking or near-field detection methods [23, 24]. The ability to produce arrays of well-separated nanopores suggests that these membranes could be used for parallel processing in high-speed sequencing [25] of large molecules and bio-species.

#### 4. Conclusions

A new generic method of nanopore preparation from self-assembled arrays of magnetic nanoparticles has been developed. The nanopores can be produced in a free-standing film or in the form of a coating. The method was demonstrated by producing HDDA membranes but it can potentially be extended to other polymerizable monomers (polymers), including biodegradable and biocompatible ones. The obtained nanopores are characterised by very unusual foam-like morphology, which offers a potential for range of applications. The viable extension of the proposed fabrication method to the micropore range has been demonstrated. As a future work, the wider range of film thicknesses could be explored, in particular in the submicron range.

#### ORCID iDs

Sergey I Rybchenko  <https://orcid.org/0000-0002-9899-313X>

#### References

- [1] Lu G Q and Zhao X S 2014 *Nanoporous Materials: Science and Engineering* (London: Imperial College Press)
- [2] Ray R T, Choi J, Bandodkar A J, Krishnan S, Gutruf P, Tian L, Ghaffari R and Rogers J A 2019 *Chem. Rev.* **119** 5461
- [3] Gao P *et al* 2011 *J. Antibiot.* **64** 625
- [4] Bernards D A and Desai T A 2010 *Soft Matter* **6** 1621
- [5] Chen Q and Liu Z 2019 *Sensors* **19** 1886
- [6] Dommelen R, Fanzio P and Sasso L 2018 *Adv. Coll. Interf. Sci.* **251** 97
- [7] Patra J K *et al* 2018 *J. Nanobiotechnol.* **16** 71
- [8] Bajpai A, Bajpai J, Saini R, Agrawal P and Tiwari A 2017 *Smart Biomat. Dev.* (Boca Raton: CRC Press)
- [9] Idrissi M E *et al* 2018 *J. Nanobiotechnol.* **16** 63
- [10] Liu J, Lawrence E M, Wu L A, Ivey M L, Flores G A, Javier K, Bibette J and Richard J 1995 *Phys. Rev. Lett.* **74** 2828
- [11] Wang H, Zhu Y, Boyd C, Luo W, Cebers A and Rosensweig R E 1994 *Phys. Rev. Lett.* **72** 1929
- [12] Flores G A, Liu J, Mohebi M and Jamasbi N 1999 *Phys. Rev. E* **59** 751
- [13] Ivey M, Liu J, Zhu Y and Cutillas S 2000 *Phys. Rev. E* **63** 011403
- [14] Hong C-Y, Jang I J, Horng H E, Hsu C J, Yao Y D and Yang H C 1997 *J. Appl. Phys.* **81** 4275
- [15] Lemaire E, Grasseli Y and Bossis G 1992 *J. Phys. II (France)* **2** 359
- [16] Cebers A 1986 *Magnitnaya Gidrodinamika (in Russian)* **16** 132
- [17] Rybchenko S, Dyab A K F, Haywood S K, Itskevich I E and Paunov V N 2009 *Nanotechnology* **20** 425607
- [18] Dyab A K F, Ozmen M, Ersoz M and Paunov V 2009 *J. Mater. Chem.* **19** 3475
- [19] Kondyurin A and Bilek M 2014 *Ion Beam Treatment of Polymers: Application Aspects from Medicine to Space* (Amsterdam: Elsevier Ltd) 978-0080994451
- [20] Edel J B and Albrecht T 2013 *Engineered Nanopores for Bioanalytical Applications* (Amsterdam: Elsevier Ltd) 978-1437734737
- [21] Nuclepore Track-etched membranes specification provided by manufacturer
- [22] Haynes W M (ed) 2010 *CRC Handbook of Chemistry and Physics* 91st edn (Boca Raton: CRC Press, Taylor & Francis Group) pp 5–73 978-1439820773
- [23] Korposh S, James S W, Lee S-W and Tatam R P 2019 *Sensors* **19** 2294
- [24] Knoll W *et al* 2020 Nanoporous thin films in optical waveguide spectroscopy for chemical analytics *Anal. Bioanal. Chem.* **412** 3299–315
- [25] Huang S, Romero-Ruiz M, Castell O K, Bayley H and Wallace M I 2015 *Nat. Nanotechnol.* **10** 986